



Cite this: *RSC Adv.*, 2019, 9, 36875

# Resin-gel incorporation of high concentrations of $W^{6+}$ and $Zn^{2+}$ into $TiO_2$ -anatase crystal to form quaternary mixed-metal oxides: effect on the a lattice parameter and photodegradation efficiency†

Lerato Hlekelele,<sup>1</sup> Shane H. Durbach,<sup>2</sup> Vongani P. Chauke,<sup>3</sup> Farai Dziike<sup>4</sup> and Paul J. Franklyn<sup>1</sup>

The search for a viable photocatalyst for water remediation is ongoing and in recent times the efforts have predominantly focused on improving the limitations of the  $TiO_2$  photocatalyst. This paper reports a dual strategy for improving the photocatalytic properties of  $TiO_2$ . The first strategy is to dope up to 30% of  $W^{6+}$  and  $Zn^{2+}$  into the crystal lattice of  $TiO_2$  using the resin gel technique to synthesize quaternary mixed metal oxides (QMMOs). It was demonstrated by laser Raman spectroscopy, PXRD and various other strategies, including dislodging the dopants from the crystal lattice of  $TiO_2$ , that these materials were successfully synthesized. More importantly, UV-DRS showed that these materials could absorb visible light.  $TiO_2$  and the QMMOs were also supported on 10% NCNTs synthesized from coal fly ash, by slightly modifying the resin gel technique. It was observed from TEM images that the NCNTs were uniformly coated with  $TiO_2$  and QMMO nanoparticles. These composites were observed to have lower photoluminescence emission spectra when compared to neat  $TiO_2$  and unsupported QMMOs. The two-part strategy employed in this project worked as the QMMOs supported on 10% NCNTs had higher visible light photodegradation efficiencies compared to neat  $TiO_2$  and the unsupported QMMOs.

Received 12th September 2019

Accepted 6th November 2019

DOI: 10.1039/c9ra07355h

[rsc.li/rsc-advances](http://rsc.li/rsc-advances)

## Introduction

Nanoscale applications of  $TiO_2$  are principally derived from its semiconductor properties, the oldest example of this is that of light aided  $H_2$  production on a  $TiO_2$  anode.<sup>1</sup> Research on nanoscale  $TiO_2$  has also been expanded to areas such as photovoltaics, photo-electrochemical sensors, medical and biomedical applications and photocatalysis for environmental conservation and water splitting.

The photoactivity of  $TiO_2$  has been shown to be reliant on its surface and crystal properties; these include morphology, surface area, polymorphic phase, lattice defects, the extent of crystallinity, particle size, the presence of uncoordinated surface sites and exposed crystal facets among other things.<sup>2-7</sup> For instance, Thuy-Duong and co-workers demonstrated the

photodegradation of methylene blue had a strong dependency on the  $TiO_2$  morphology;  $TiO_2$  in the shape of a flower containing rutile nano-prisms adhered by anatase nanoparticles showed the best photodegradation efficiency whereas the material with a hierarchical cauliflower morphology had the least photoactivity.<sup>8</sup> In another study, He *et al.* demonstrated how the morphology of  $TiO_2$ , its crystal size, and calcination progress affected the photodegradation of gaseous benzene.<sup>9</sup>

Another strategy of improving the photocatalytic properties of  $TiO_2$  is by compositing it with other materials like zeolites (molecular sieves), carbon nanomaterials, fly ash, stainless steel, glass, silica, polymers, and zeolites among other materials.<sup>10-16</sup> In instances where  $TiO_2$  is supported on steel and glass, the aim is usually for just immobilizing the  $TiO_2$  nanoparticles to ensure it is easy to separate them from treated water.<sup>10,17,18</sup> On the other hand, materials such as zeolites and carbon nanomaterials (CNMs) (including nitrogen-doped carbon nanotubes (NCNTs)) are used as functional materials; they improve the photocatalytic activity of  $TiO_2$  by trapping the photo-induced electrons thus separating the active charge carriers.<sup>12,14,19,20</sup>

Surface doping of  $TiO_2$  with metal nanoparticles has also been shown to be an effective way of improving the photocatalytic efficiency of  $TiO_2$ . Zero-valent transition metals have

<sup>1</sup>Molecular Science Institute, School of Chemistry, University of the Witwatersrand, Johannesburg, 2050, South Africa. E-mail: LHlekelele@csir.co.za

<sup>2</sup>DST-NRF Centre of Excellence in Strong Materials, University of the Witwatersrand, WITS, 2050, Johannesburg, South Africa

<sup>3</sup>Polymers and Composites, Materials Science and Manufacturing, Council for Scientific and Industrial Research, P. O. Box 395, 0001, Pretoria, South Africa

† Electronic supplementary information (ESI) available. See DOI: 10.1039/c9ra07355h



been loaded onto TiO<sub>2</sub> in attempts to improve its photocatalytic efficiencies.<sup>21,22</sup> Dziilke *et al.* reported that the photocatalytic activity of TiO<sub>2</sub> was increased by loading Ni nanoparticles onto it and attributed the increase in activity to the separation of the active charge carriers.<sup>3</sup> This occurs because the Fermi level of TiO<sub>2</sub> is higher than that of most of the metal nanoparticles commonly used for this purpose, so the electrons migrate from TiO<sub>2</sub> to the metal nanoparticles resulting in a space charge layer at the boundaries between TiO<sub>2</sub> and the metal nanoparticles. The electric field created drives the electrons to the inside and the holes are drawn to the interfacial region of TiO<sub>2</sub>.<sup>22</sup> Therefore, in setups like this, metal nanoparticles act as electron sinks thus resulting in the efficacy of the charge carrier separation and subsequent inhibition of recombination.<sup>21–23</sup> This is also applicable for noble metal nanoparticles.<sup>3,16,24–27</sup> Additionally, when noble metals are dispersed on the surface of TiO<sub>2</sub>, a plasmonic composite can be formed that allows the material to be able to absorb visible light by surface plasmon resonance (SPR).<sup>3,16,28–30</sup>

Other scientists have investigated compositing TiO<sub>2</sub> with other photocatalytic (semiconductors) materials such as ZnO, NiO, WO<sub>3</sub>, and Fe<sub>2</sub>O<sub>3</sub>.<sup>31,32</sup> WO<sub>3</sub> is one of the semiconductors that have attracted much attention for compositing with TiO<sub>2</sub>. Both Do *et al.* and Know *et al.* have tested the photoactivity of TiO<sub>2</sub>/WO<sub>3</sub> for the photodegradation of dichlorobenzene under UV-light, and reported superior activities for these composites compared to that of TiO<sub>2</sub> alone.<sup>33,34</sup> Here, the enhanced activity was due to the electron band positions of WO<sub>3</sub> and TiO<sub>2</sub> having been favorably positioned for charge separation. The photoactivity of TiO<sub>2</sub>/WO<sub>3</sub> composites have also been measured under visible radiation, as the bandgap of WO<sub>3</sub> is narrower (2.8 eV), and was shown to be superior to that of individual WO<sub>3</sub> and TiO<sub>2</sub> under visible light.<sup>25,31,35</sup> ZnO is another semiconductor that has UV-light photoactivity that has rivaled that of TiO<sub>2</sub>, however, it has been shown to suffer from photocorrosion which significantly reduced its activity and stability.<sup>36,37</sup> Fang-Xing Xiao synthesized ZnO–TiO<sub>2</sub> nanotubes (TNTs) that were highly ordered and had photoactivity that was higher than that of ZnO and TiO<sub>2</sub> separately.<sup>38</sup> Here the increased activity was attributed to better charge separation. It was suggested that holes accumulated at the valence band of ZnO and electrons accumulated at the conduction band of TiO<sub>2</sub> so that migration could occur with minimal recombination.<sup>31,37–39</sup>

The abovementioned examples have focused on the formation of mixtures of metal oxides, where a great deal of research has been performed. On the contrary, less research has been focused on the synthesis and use of TiO<sub>2</sub>-based mixed metal oxides by introducing foreign metal ions into its crystal lattice structure for use in photocatalysis. In order to achieve this, it is important that the crystal structure of TiO<sub>2</sub> be understood in order to systematically introduce foreign metal ions into its crystal lattice. One of the important crystal structural properties of anatase is that the atoms are comparatively loosely packed with fairly large vacancies thus the anatase phase has the ability to hold multiple cation oxidation states and environments.<sup>40–43</sup> This makes it possible to introduce other metal ions into the anatase crystal, through replacement of Ti ions and/or vacancy occupation.

In this research, the incorporation of Zn<sup>2+</sup> and W<sup>6+</sup> into the crystal lattice of TiO<sub>2</sub> using a novel resin gel method to form quaternary mixed metal oxides (QMMOs) is reported. Franklyn and Narrandes have demonstrated the applicability of the resin gel synthesis technique for the synthesis of TiO<sub>2</sub>.<sup>44</sup>

## Experimental

### Synthesis of QMMOs

The principles of the resin gel technique are described by Franklyn and Narrandes.<sup>44</sup> An appropriate volume of TiCl<sub>4</sub> (Fluka) was measured and dissolved in 10 ml ethanol (Sigma Aldrich) kept at 0 °C using ice whilst stirring magnetically. An appropriate mass of Zn(NO<sub>3</sub>)<sub>2</sub>·4H<sub>2</sub>O (Merck) was weighed and dissolved in 10 ml ethanol by stirring. Having made the ethanoic Zn<sup>2+</sup> solution, 50 g of polyethylene glycol, *M<sub>w</sub>* 8.000 g mol<sup>−1</sup> (Sigma Aldrich) was added to it, heated to 150 °C whilst stirring until all the polymer had dissolved. The W<sup>6+</sup> solution was prepared by dissolving an appropriate mass of H<sub>2</sub>WO<sub>4</sub> (Sigma Aldrich) in 10 ml NH<sub>4</sub>OH (Sigma Aldrich). The Ti<sup>4+</sup> solution was added to the W<sup>6+</sup> solution and stirred for 5 min and the solution consisting of Zn<sup>2+</sup> and PEG was added to the mixture and stirred for a further 60 min. The white viscous homogenous solution that formed was then placed under a 200 W incandescent lamp until it was completely desolvated and a hard wax had formed. The samples were then transferred into ceramic crucibles, placed on a sand bath and heated to 300 °C. Here, the sample liquefied. The temperature of the sand bath was then increased to 400 °C, where some of the samples ignited. The samples that had not ignited were burned from above with a Bunsen burner to induce ignition. The burning of the samples was allowed to go on until the flames ceased by themselves at which point the samples were now in the form of black granular powder.

The samples were then calcined at 400 °C for 12 h in the air to crystallize the particles and remove the soot. The calcination conditions were optimized where it was realized that 400 °C for 12 h was optimal; calcining at higher temperatures resulted in undesirable phase transformation, whereas lower temperatures were not suitable for the complete removal of soot.

The metal ion ratios (Ti<sup>4+</sup>:W<sup>6+</sup>:Zn<sup>2+</sup>) of the samples prepared were: (9 : 1 : 0), (9 : 0 : 1), (8 : 2 : 0), (8 : 1 : 1), (8 : 0 : 2), (7 : 3 : 0), (7 : 2 : 1), (7 : 1 : 2) and (7 : 0 : 3). The pure metal oxides were prepared following the same procedure as for the mixed metal oxides except that the solvents were added without the other metal precursor(s), *i.e.* TiO<sub>2</sub> was synthesized in exactly the same way as QMMOs except for that H<sub>2</sub>WO<sub>3</sub> and Zn(NO<sub>3</sub>)<sub>2</sub>·4H<sub>2</sub>O were not added to the mixture. Such was the case for the synthesis of WO<sub>3</sub> and ZnO. The pure metal oxides and QMMOs that were calcined at 400 °C for 12 h in the air were labeled as described in Table S1.†

### Synthesis and purification of NCNTs

The description of the synthesis and purification processes of the NCNTs that were used in this study have been described in our previous reports.<sup>19,45</sup> Concisely, a two-stage quartz tube furnace with independent thermocouples and controllers was



used for the synthesis of NCNTs. A gram of the carbon and nitrogen source, melamine (Sigma Aldrich), was placed in a quartz boat and placed in the middle of the first-stage furnace. The coal fly ash catalyst (0.5 g, from Eskom) in a quartz boat was then placed in the middle of a second-stage furnace.

The second-stage furnace containing CFA was heated to 900 °C (ramped at 10 °C min<sup>-1</sup>) whilst N<sub>2</sub>(g) (AFROX) was flowing (flow rate of 50 ml min<sup>-1</sup>) into the quartz tube reactor, in through the first furnace and out the second furnace. Once the second stage furnace had reached 900 °C, the temperature of the 2<sup>nd</sup> stage was heated to 350 °C in 10 min (35 °C min<sup>-1</sup>). At this temperature, melamine was vaporized and its fumes were carried into the second stage furnace by nitrogen gas for the growth of the NCNTs.

The as-prepared NCNTs were stirred in 20 ml of 5% HF (HF Chemicals) aqueous solution for 24 h at room temperature. The mixture was diluted with 150 ml of distilled water, centrifuged and washed several times with water. The wet mud was transferred into a round bottom flask that contained 30 ml HNO<sub>3</sub>, 10 ml H<sub>2</sub>SO<sub>4</sub> (both Sigma-Aldrich) and 60 ml water and heated at 60 °C for 12 h.

This was followed by compositing the various QMMOs with NCNTs. Here, the resins were synthesized as described above except that in this instance they were prepared in the presence of NCNTs and were not ignited. An amount of NCNTs corresponding to 10% (m/m) of NCNTs relative to that of the various QMMOs or TiO<sub>2</sub>, was added to the white homogeneous solution of QMMOs or TiO<sub>2</sub> and stirred magnetically for 2 h until a grey homogeneous mixture was formed. The mixtures were then transferred into pressure sealed autoclaves lined with Teflon to complete the reactions at 150 °C for 12 h. Grey precipitates were collected, centrifuged and washed with distilled water. The resulting materials were then calcined at 400 °C for 12 h to remove the soot.

### Materials characterization

The materials, *i.e.* pure metal oxides and the various QMMOs and NCNTs based composites were characterized using several characterization techniques. The crystallization of the materials was characterized by powder X-ray diffraction (PXRD) at 2θ position ranging between 10 and 90° using a Bruker D2 phaser (Bruker AXS, Karlsruhe, Germany) in Bragg–Brenton geometry with a Lynx detector using Co-Kα radiation at 30 kV and 10 mA. The crystallization of the materials was also studied by laser Raman spectroscopy at an excitation wavelength of 517 nm recorded by means of a Jobin-Yvon T64000 Raman spectrometer equipped with an Olympus BX40 microscope. Transmission electron microscopy (TEM) was used to study the morphological properties of the materials. The TEM used is called an FEI Tecnai G2 Spirit electron microscope (FEICo., Hillsboro, OR, USA) at an accelerating voltage of 120 kV. The TEM is also coupled to an energy-dispersive X-ray spectrometer (EDS) which was used for elemental analysis. UV-vis diffuse reflectance spectroscopy (DRS) was used to study the optical properties. The measurements were done on a commercial Praying Mantis DRS Cary 500. The presence of NCNTs in the composites was also

studied using thermogravimetric analysis (PerkinElmer Pyris). The samples were heated from ambient temperature to 900 °C at 10 °C min<sup>-1</sup> in air. Photoluminescence spectroscopy studies were done on the same instrument as laser Raman spectroscopy measurements, at an excitation wavelength of 290 nm. Scanning electron microscopy (SEM) coupled to EDS analyses were carried out on a Zeiss Crossbeam 540 FEG. Photocurrent measurements were done on a potentiostat/galvanostat using a three-electrode system comprising of an Ag/AgCl reference electrode, a platinum wire counter electrode and a fluoride doped titanium glass working electrode in a 0.1 M K<sub>2</sub>SO<sub>4</sub> (Merck) supporting electrolyte solution. The working electrode was prepared by mixing 10 parts polyvinylidene difluoride (Sigma-Aldrich) with 1 part TWZ721/10% NCNTs to form a paste which was then applied to the working electrode. The electrode was then allowed to dry in an oven for 5 h at 120 °C at which point a copper wire was attached to it using a silver paste. The electrode was kept at room temperature overnight to allow the paste to dry before it was used.

### Photocatalytic testing

The photoactivities of these materials were evaluated by the photodegradation of BPA. This was done as reported in our previous reports.<sup>16,19</sup> The process is described in the ESI (S2†).

## Results and discussion

### Characterization of pure metal oxides

The pure metal oxides, WO<sub>3</sub>, ZnO and TiO<sub>2</sub>-anatase were studied and confirmed by PXRD (Fig. S1†), TEM (Fig. S2a, S3a and S4a†), EDS (Fig. S2c, S3c and S4c†) and laser Raman spectroscopy. Here it was concluded that the resin gel technique yielded desirable and uncontaminated materials, although trace amounts of carbon attributed to the unburned soot were detected.

### Characterization of QMMOs

**PXRD analyses of QMMOs.** PXRD analyses were conducted on the QMMOs and their patterns were compared to the pattern of TiO<sub>2</sub>. The PXRD patterns of the various QMMOs were similar to that of the TiO<sub>2</sub>-anatase phase, indicating that Zn<sup>2+</sup> and W<sup>6+</sup> were incorporated into the TiO<sub>2</sub> crystal lattice without any phase change (Fig. 1a). This was justified on the basis of the argument put forward by Franklyn.<sup>46</sup> The crystal radii of Ti<sup>4+</sup>, W<sup>6+</sup>, and Zn<sup>2+</sup> are similar when in a six coordination geometry. Therefore, the three metal ions should be entirely harmonious with each other when in one crystal structure. Franklyn went on to suggest that it was likely that the incorporation of W<sup>6+</sup> and Zn<sup>2+</sup> with different charges to that of Ti<sup>4+</sup> should change the crystal radius of oxygen ions because of basic electronic effects. This then led to the assumption that, in our work, the incorporation of these metal ions into the TiO<sub>2</sub> (anatase) should bring about changes in the unit cell *i.e.* the local lattice should be distorted. Indeed, this is true in this work as it was observed that the (101) reflection of the QMMOs appeared at higher 2θ values relative to that of TiO<sub>2</sub> (Fig. 1b).



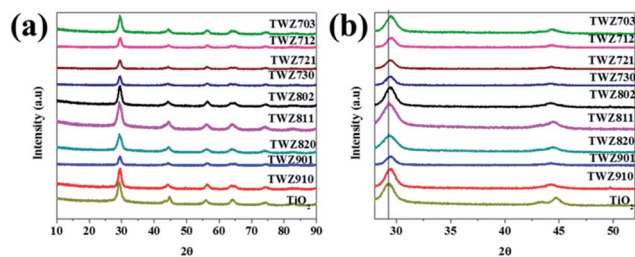


Fig. 1 (a) PXRD patterns of TiO<sub>2</sub> and various QMMOs and (b) inset showing the (101) and (004) reflections of TiO<sub>2</sub> and various QMMOs.

In addition to the variations in the  $2\theta$  position of the (101) reflection of QMMOs relative to that of TiO<sub>2</sub>, similar variations were also observed amongst the different QMMOs (Fig. 1 and Table 1). It was observed that the  $2\theta$  value of the (101) reflection of the QMMOs increased with an increasing percentage of dopants. The (101) reflections of QMMOs containing 90% Ti<sup>4+</sup> appeared at  $2\theta$  values closer to that of TiO<sub>2</sub> whereas those that contained 70% Ti<sup>4+</sup> were observed at considerably higher  $2\theta$  values relative to that of TiO<sub>2</sub>.

Furthermore, it was observed that the (101) reflection of QMMOs containing more W<sup>6+</sup> relative to Zn<sup>2+</sup> appeared at higher  $2\theta$  values. This indicated that W<sup>6+</sup> ions distorted the TiO<sub>2</sub> lattice at a higher degree than Zn<sup>2+</sup>.

The degree of distortions that occurred on the crystal lattice of TiO<sub>2</sub> as a result of incorporating W<sup>6+</sup> and Zn<sup>2+</sup> was estimated by means of calculating the lattice parameters. The lattice parameters were calculated by measuring accurately the  $2\theta$  positions of the (004) and (001) peaks. The  $a$  lattice parameter of the QMMOs are different from that of TiO<sub>2</sub>. The  $a$  lattice parameter of the QMMOs also varies amongst the different QMMOs. The QMMOs that contained 90% Ti<sup>4+</sup> had lattice parameters that were closer to that of TiO<sub>2</sub>, followed by those that contained 80% Ti<sup>4+</sup> and those that contained 70% Ti<sup>4+</sup> differed the most to that of TiO<sub>2</sub>. Furthermore, the  $a$  lattice parameters of the QMMOs were observed to vary with varying amounts of W<sup>6+</sup> and Zn<sup>2+</sup> when comparing a series of QMMOs with the same Ti<sup>4+</sup> concentration, e.g. the  $a$  lattice parameter of TWZ730 was lower than that of TWZ721 which was in turn lower than that of TWZ712 (Table 1).

Table 1 Summary of the particle sizes, (004) and (101) reflection positions and lattice parameters of TiO<sub>2</sub> and the various QMMOs

Sample	Particle size		Lattice parameters		
	$2\theta$ (004)/°	$2\theta$ (101)/°	(nm)	$a$ (pm)	$c$ (pm)
TiO <sub>2</sub>	44.732	29.275	10.5	490.077	808.121
TWZ910	44.416	29.338	11.7	485.644	815.854
TWZ901	44.479	29.316	11.2	486.603	814.757
TWZ820	44.469	29.465	12.3	483.547	812.555
TWZ811	44.606	29.461	12.8	482.811	814.930
TWZ802	44.484	29.405	12.6	484.694	813.663
TWZ730	44.479	29.576	13.3	481.053	815.087
TWZ721	44.479	29.546	13.4	480.983	815.070
TWZ712	44.460	29.531	13.2	480.713	814.757
TWZ703	44.461	29.528	13.2	479.955	814.757

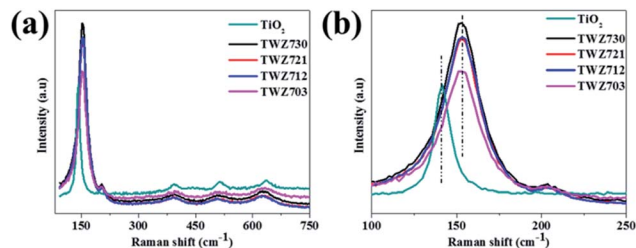


Fig. 2 (a) Laser Raman spectra of TiO<sub>2</sub> and QMMOs and (b) inset showing the E<sub>g</sub> peak.

The PXRD patterns of TiO<sub>2</sub> and the various QMMOs were used to calculate their particle size. The Scherrer's equation using the (101) reflection was used for this purpose where it was found that TiO<sub>2</sub> nanoparticles are smaller than all the QMMOs particles. Additionally, the size of the QMMOs metal oxide particles increased with decreasing amount of Ti<sup>4+</sup>.

**Laser Raman analyses of QMMOs.** It was observed from PXRD measurements that variations between TiO<sub>2</sub> and QMMOs are more pronounced in the case of QMMOs that contained 70% Ti<sup>4+</sup>. For this reason, it was determined that further characterization of these materials was necessary.

The laser Raman signatures of TiO<sub>2</sub> and the QMMOs consisting of 70% Ti<sup>4+</sup> were studied. It was observed that the laser Raman signatures of the QMMOs were similar to that of TiO<sub>2</sub> (Fig. 2a). This was consistent with what was observed from PXRD measurements. Furthermore, closer investigations of the E<sub>g</sub> peaks of the QMMOs and TiO<sub>2</sub> showed that the E<sub>g</sub> peaks of the QMMOs had shifted to shorter wavelengths relative to that of TiO<sub>2</sub>, a phenomenon that was observed in PXRD measurements, where the (101) PXRD reflections of the QMMOs were at higher  $2\theta$  values relative to that of TiO<sub>2</sub>. This also indicates that the incorporation of W<sup>6+</sup> and Zn<sup>2+</sup> ions into the lattice of TiO<sub>2</sub> resulted in lattice distortions (Fig. 2b).

**TEM and EDS of QMMOs.** TEM and EDS analyses were also conducted on QMMOs consisting of 70% Ti<sup>4+</sup> as shown in Fig. 3. The QMMOs were found to all have similar morphologies (Fig. 3a–d) which was similar to that of TiO<sub>2</sub> (Fig. S4a†). This was consistent with laser Raman and PXRD data where it was found that TiO<sub>2</sub> and the QMMOs had similar laser Raman spectral and diffraction features. This further confirmed that W<sup>6+</sup> and Zn<sup>2+</sup> ions were incorporated into the lattice of TiO<sub>2</sub> as opposed to forming a mixture of metal oxides. This conclusion was also reached in part because the morphological properties of ZnO and WO<sub>3</sub> vary from those of TiO<sub>2</sub> and QMMOs (see Fig. S2a and S3a†).

On the other hand, the EDS spectra of the various QMMOs were found to differ amongst themselves (Fig. 3e and f) and were different from that of TiO<sub>2</sub> (Fig. 4c). The EDS spectrum of TWZ730 consisted of elemental Ti, W, and O (Fig. 3e). The same case was observed with the other QMMOs; in the case of TWZ703 no peaks associated with W were present but those of Zn were observed. The other two QMMOs, TWZ712 and TWZ721 had similar EDS spectra showing the presence of elemental Ti, W, Zn, and O.



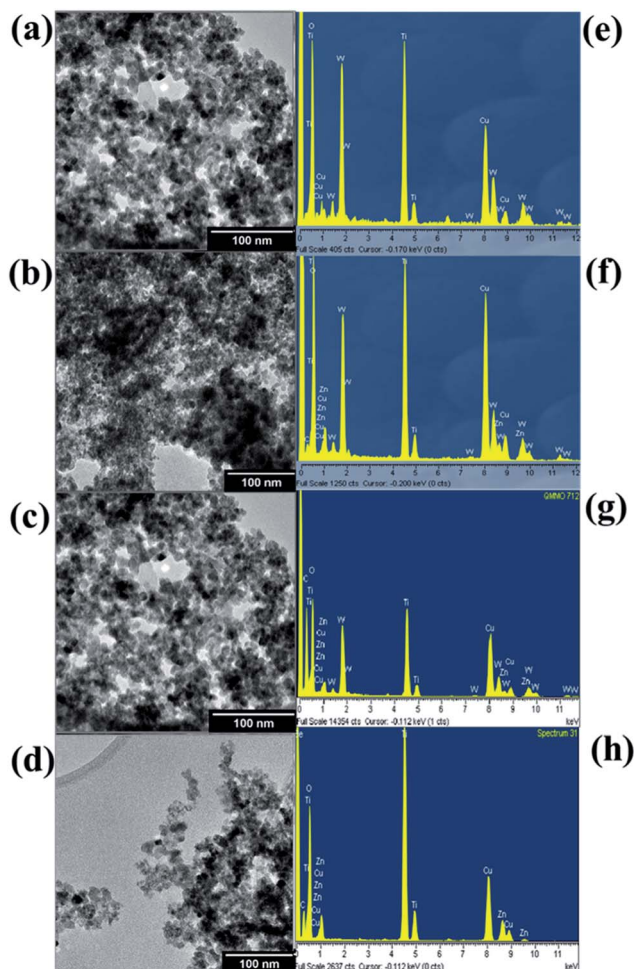


Fig. 3 TEM images of (a) TWZ703, (b) TWZ712, (c) TWZ721 and (d) TWZ730. EDS spectrum of (e) TWZ703, (f) TWZ712, (g) TWZ721 and (h) TWZ730.

In order to further investigate the presence of tungsten and zinc atoms in the  $\text{TiO}_2$  crystals SEM and EDS mapping analyses were conducted on TWZ721 (Fig. 4). Here, it was observed that

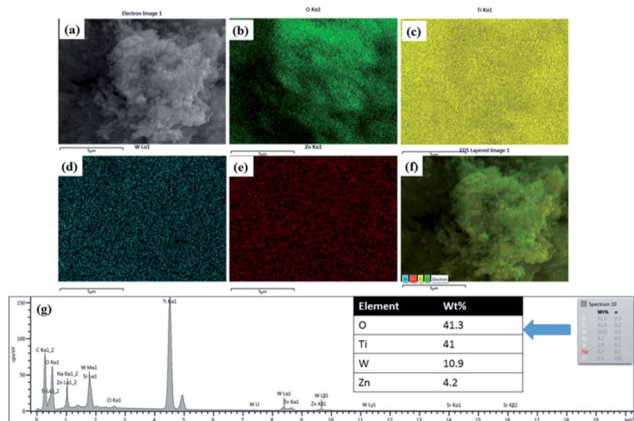


Fig. 4 (a) SEM image of TWZ721, EDS elemental maps of (b) oxygen, (c) titanium, (d) tungsten, (e) zinc, (f) EDS layered image of Ti, Zn, O and W, and (g) EDS spectra of TWZ721.

the various elements, Ti, W, Zn, and O were uniformly distributed throughout the sample, in all the crystals even though they differed in amount. This observation also proved that Zn and W ions were incorporated into the crystal lattice of  $\text{TiO}_2$ . The elemental ratio of the 3 cations was calculated from the EDS spectrum of sample TWZ721 and was found to be T(73%) : W(19%) : Zn(8%). This was adjudged to be a fair approximation of the sample composition given the quantitative shortcomings of EDS.

**Characterization of pure metal oxides and QMMOs calcined at 800 °C.** Calcining the pure metal oxides at 800 °C induced a phase change for  $\text{TiO}_2$  and  $\text{WO}_3$  whereas no such phase change was observed in the case of ZnO (Section S6 and Fig. S8a–c†). This is useful as it was used to test the hypothesis that converting  $\text{TiO}_2$  from anatase to rutile will result in the removal of the  $\text{W}^{6+}$  and  $\text{Zn}^{2+}$  ions from the  $\text{TiO}_2$  lattice. Therefore, this could potentially further demonstrate that the QMMOs were formed.

In order to investigate this hypothesis, PXRD analyses were performed on the QMMOs consisting of 70%  $\text{TiO}_2$  that were calcined at 800 °C to induce phase transformation of the  $\text{TiO}_2$ -anatase phase to the rutile phase (Fig. 5). The PXRD patterns of the calcined QMMOs were different from those of the uncalcined materials. Furthermore, when compared to that of  $\text{TiO}_2$  calcined at 800 °C, their patterns consisted of matching rutile peaks but also consisting of several other peaks which were those of W, Zn oxides and probably other alloys, further demonstrating the QMMOs were formed and that the more thermodynamically stable rutile phase of  $\text{TiO}_2$  cannot accommodate high levels of  $\text{W}^{6+}$  and  $\text{Zn}^{2+}$  dopants.

**UV-vis DRS  $\text{TiO}_2$  and QMMOs.** The preceding discussed data gave a strong indication that the incorporation of  $\text{W}^{6+}$  and  $\text{Zn}^{2+}$  had been achieved. In order to ascertain if this had any effect on the optical properties of  $\text{TiO}_2$ , UV-DRS analyses were conducted (Fig. 6). It was observed from the UV-DRS spectra of  $\text{TiO}_2$  and the QMMOs that all the materials had sharp absorption edges in the 400–450 nm region. The bandgap of  $\text{TiO}_2$  was approximated to be lower than those of the QMMOs whereas the band gaps of the various QMMOs were found to decrease with

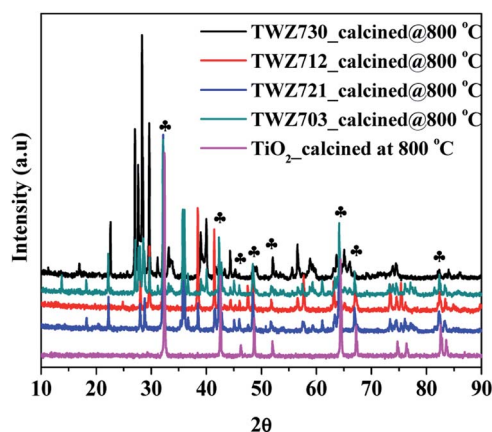


Fig. 5 PXRD patterns of  $\text{TiO}_2$  and the various QMMOs calcined at 800 °C.

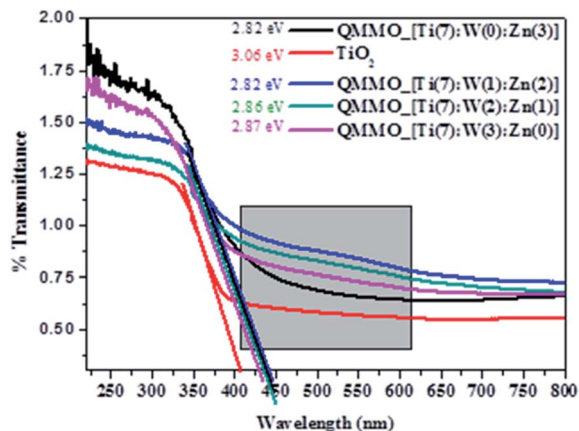


Fig. 6 UV-DRS spectra of TiO<sub>2</sub> and QMMOs.

increasing amounts of zinc ions incorporated. Furthermore, it was observed that the UV-DRS spectrum of TiO<sub>2</sub> was flat from 400 nm whereas those of the QMMOs had a wide absorption band extending up to 600 nm. This indicated that the presence of W<sup>6+</sup> and Zn<sup>2+</sup> in the lattice of TiO<sub>2</sub> influenced its electronic structure such that a new conduction band was created. This is desirable as it meant that it was possible that the materials could harvest visible light and as such could be used for visible light-driven photocatalysis.

**Characterization of TiO<sub>2</sub> and QMMOs loaded on 10% NCNTs.** TEM analyses were conducted on the composites in order to ascertain if the coating of the NCNTs with TiO<sub>2</sub> or QMMOs nanoparticles was achieved. Indeed, it was observed on the TEM images of these composites as shown in Fig. 7 that the NCNTs were coated uniformly with nanoparticles. This was deemed to be desirable as it increased the likelihood of forming a heterojunction between the NCNTs and QMMOs/TiO<sub>2</sub> that could possibly reduce the recombination of electrons and holes thus increasing the photocatalytic efficiency of the materials.<sup>47</sup>

PXRD analyses were performed on these composites to ensure that the process of compositing TiO<sub>2</sub> and the various QMMOs with NCNTs did not change the crystallographic structure of the nanoparticles (Section S7, Fig. S9a and b†). Here, it was observed and confirmed that TiO<sub>2</sub> and the QMMOs loaded onto had the crystal structure of TiO<sub>2</sub>-anatase.

The composites were studied by TGA in order to ascertain if indeed the composites consisted of both inorganic metal oxides and carbonaceous materials. Here, it was observed that *ca.* 10% of the various materials were combusted in air at temperatures below 700 °C. This showed that the materials contained approximately 10% NCNTs (Section S8 and Fig. S10†) and 90% metal oxide.

Having established that TiO<sub>2</sub> and QMMOs were successfully loaded onto NCNTs, photoluminescence analyses were conducted in order to ascertain if they had any effect on the recombination of the photo-induced charge carriers. The photoluminescence emission peaks of TiO<sub>2</sub>, QMMOs, and composites were compared against each other (Fig. 8). The emission peaks were observed upon exciting the materials with

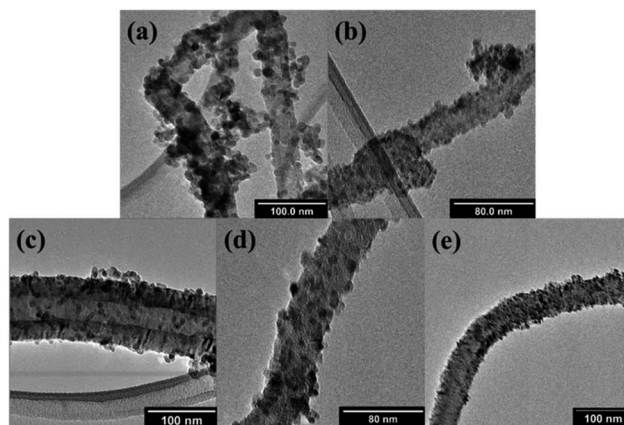


Fig. 7 TEM images of (a) TiO<sub>2</sub>/10% NCNTs, (b) TWZ730/10% NCNTs, (c) TWZ721/10% NCNTs, (d) TWZ712/10% NCNTs and (e) TWZ703/10% NCNTs.

radiation with a wavelength of 290 nm. The emission intensity of TiO<sub>2</sub> was the highest observed indicating the lifetime of its electrons and holes was short. The intensities of the QMMOs were lower than that of TiO<sub>2</sub> indicating that the incorporation of W<sup>6+</sup> and Zn<sup>2+</sup> decreased the recombination rate of the photo-induced charge carriers.

Furthermore, it was observed that the emission intensity of QMMOs decreased with the decreasing amount of W<sup>6+</sup> (decreasing the amount of Zn<sup>2+</sup>) such that the emission intensity of the QMMO without W<sup>6+</sup> TWZ703 was significantly lower than that of the QMMO with 30% W<sup>6+</sup> TWZ730. This indicated that the incorporation of Zn<sup>2+</sup> was more effective at reducing the charge carriers' recombination rate. The materials composited with 10% NCNTs had significantly lower than those of QMMOs and TiO<sub>2</sub>. This was attributed to the NCNTs which are able to quench photoinduced electrons thus reducing the possibility of these electron recombining with holes.<sup>15,48–50</sup>

### Photocatalytic testing

Prior to all photodegradation experiments, two control experiments were conducted: (i) BPA (80 ppm, 50 ml) was stirred in the presence of the various photocatalysts in the dark for 6 h. Here, it was observed that the adsorption equilibrium of BPA onto the various photocatalysts was 2 h and very low amounts of

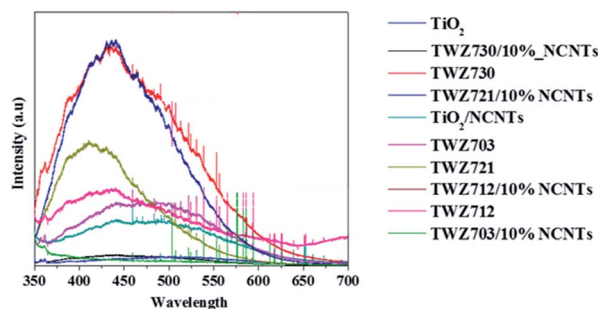


Fig. 8 Photoluminescence emission spectra of TiO<sub>2</sub>, QMMO, and composites.



BPA were adsorbed by the various photocatalysts (maximum 1.5%). (ii) The second control experiment was conducted in order to investigate the photolysis of BPA, *i.e.* the photo-degradation of BPA in the absence of a catalyst. Here, BPA was irradiated with visible light from a solar simulator for 2 hours and it was found that there was essentially no reduction in BPA concentration (less than 0.5% reduction).

In the case of photocatalytic degradation studies, adsorption equilibrium of the test sample (80 ppm, 50 ml BPA) onto the various materials was first established in 2 h (Table 2) before irradiating. The photocatalytic activity (after radiating) of neat TiO<sub>2</sub> was found to be the lowest when compared to those of the QMMOs and the carbon-based composites (Table 2, Section S9 and Fig. S11†). The low photoactivity was attributed to the fact that unmodified TiO<sub>2</sub> does not absorb visible light.

In the case of QMMOs, it was observed that their photocatalytic activities (ranged between 32 and 46%) were higher than that of TiO<sub>2</sub>. The increased photocatalytic activities were attributed to that the QMMOs absorbed visible light (Fig. 6) and they had somewhat lower photoluminescence emission peaks (Fig. 8). Furthermore, it was observed that the photocatalytic activities of the QMMOs increased with increasing amounts of Zn<sup>2+</sup> incorporated (decreasing amount of W<sup>6+</sup> incorporated).

Regarding the NCNTs-based composites, it was observed that supporting TiO<sub>2</sub> onto NCNTs did not increase photocatalytic degradation in a significant way, only by 6% ( $X_{60 \text{ min}} = 30\%$ ). This is because loading TiO<sub>2</sub> onto NCNTs did not affect the bandgap of TiO<sub>2</sub> in any substantial way, as we had previously reported.<sup>19</sup> Nevertheless, compositing TiO<sub>2</sub> with NCNTs increased the lifetime of the few active charge carriers that were created, evidence being that the photoluminescence emission peak of TiO<sub>2</sub>/10% NCNTs was lower than that of TiO<sub>2</sub> (Fig. 8). On the other hand, the QMMOs supported onto NCNTs had the highest photocatalytic activities ranging between 89–91%. This is as a result of the combined effect of that incorporating Zn<sup>2+</sup> and W<sup>6+</sup> introduced mid-band gap energies thus making it possible for the materials to absorb visible light and the increased lifetime of the active charge carriers (Fig. 6).

Table 2 Photocatalytic efficiency of the various materials

Photocatalyst	% removal (2 h adsorption equilibrium)	% removal (after 60 min photocatalysis)
TiO <sub>2</sub>	0.9	26.51
TWZ730	0.7	32.535
TWZ721	0.8	37.535
TWZ712	0.8	39.535
TWZ703	0.9	42.535
TiO <sub>2</sub> /10% NCNTs	1.4	29.51
TWZ730/10%	1.5	88.558
NCNTs		
TWZ721/10%	1.4	89.998
NCNTs		
TWZ712/10%	1.4	90.92
NCNTs		
TWZ703/10%	1.5	90.42
NCNTs		

The reported method of synthesis has not been used to incorporate large amounts of dopants into TiO<sub>2</sub>-anatase and supporting the nanoparticles onto NCNTs. Nevertheless, there are several other reports that are beneficial for putting this current work into context, particularly for drawing up a mechanism. First, in the case of incorporating W<sup>6+</sup> and Zn<sup>2+</sup> into TiO<sub>2</sub>-anatase or similar work, García *et al.* reported the incorporation of up to 3% W<sup>6+</sup> (and Mo<sup>6+</sup>) using the evaporation induced self assembly method.<sup>51</sup> They showed by PXRD that the (101) TiO<sub>2</sub>-anatase had shifted and that the crystal lattice of TiO<sub>2</sub>-anatase had been distorted, proving the incorporation of these metal ions as it is shown in this work. Perhaps, more importantly, they reported that incorporating W<sup>6+</sup> did not significantly narrow the absorption edge of TiO<sub>2</sub>-anatase. This is similar to what is observed in this work that the band gaps of QMMOs with higher amounts of W<sup>6+</sup> were closer to that of pure TiO<sub>2</sub>-anatase (Fig. 6). They attributed this to that the 5d levels of tungsten ions were probably inside (or just below) the conduction band of Ti 3d conduction band.<sup>51,52</sup> Nevertheless, there was an observable reduction in bandgap (TiO<sub>2</sub> 3.06 and TWZ 2.87 eV, Fig. 6) and this is attributable to new states created just below the conduction band of TiO<sub>2</sub> (Fig. 9). This transition is labeled  $h\nu_2$  in Fig. 9.

In the case of doping Zn<sup>2+</sup> into TiO<sub>2</sub>-anatase, Benjwal *et al.* used the sol-gel method to dope up to 2% Zn<sup>2+</sup> into TiO<sub>2</sub>-anatase and proved it by XRD, XPS, and TEM.<sup>53</sup> They observed that this exercise yielded materials with a bandgap narrower than that of pure TiO<sub>2</sub> just as it was observed in this work (Fig. 6). In this case, also, the reduction in band gap was attributed to the creation of new states below the conduction band of TiO<sub>2</sub> and probably slightly below the position of the 5d level of tungsten (labeled as  $h\nu_3$  on Fig. 9) as the bandgap was visibly narrower for QMMOs that contained more zinc than tungsten ions (Fig. 6).

In addition to the slight shifts in the bandgap of the QMMOs relative to pure TiO<sub>2</sub>, there are obvious broad peaks on between 400 and 600 nm on the spectra of the QMMOs that are not present on the TiO<sub>2</sub> spectrum (Fig. 6). These were attributed to the possible transitions between the conduction band of TiO<sub>2</sub> and the various states below it. The transitions are labeled as  $h\nu_4$  and  $h\nu_5$  on Fig. 9.

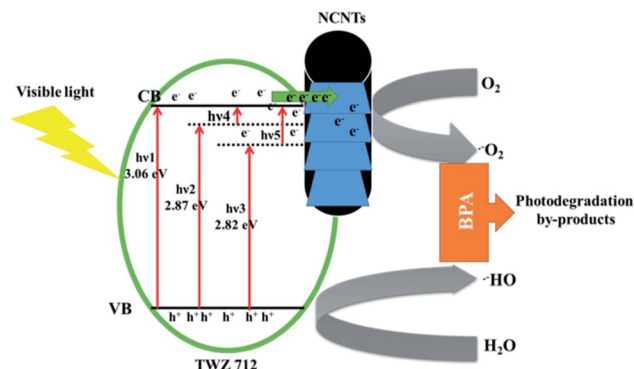


Fig. 9 Proposed BPA photocatalytic mechanism using TWZ721/10% NCNTs.



Nitrogen-doped carbon nanotubes play a well-documented role in the BPA degradation process. It serves as a sink for electron to aid the separation of charge carrier thus improving the photocatalytic efficiency (Fig. 9), of the material, one of many useful functions of nanocarbon materials.<sup>19,47,54,55</sup> The evidence for this was observed from photoluminescence studies where it was observed that the electron/hole recombination rate was significantly shortened by compositing the QMMOs/TiO<sub>2</sub> with NCNTs (Fig. 8).

## Conclusion

W<sup>6+</sup> and Zn<sup>2+</sup> ions were successfully incorporated into the crystal lattice of TiO<sub>2</sub> (anatase phase) using the resin gel technique to form QMMOs. This was confirmed using various characterization techniques, including PXRD, EDX, TEM, and laser Raman spectroscopy. The calcination of the QMMOs at 800 °C in air resulted in the material decomposing into tungsten trioxide, zinc oxide and the rutile phase of TiO<sub>2</sub>, further confirming that mixed metal oxides were formed. The incorporation of these metal ions into the lattice of TiO<sub>2</sub> did not alter the band edge of TiO<sub>2</sub> as was shown by UV-DRS but a wide absorption band was observed in the case of the QMMOs which wasn't there for TiO<sub>2</sub>. Composites consisting of QMMOs/TiO<sub>2</sub> and NCNTs (10% loading) were successfully synthesized by modified resin gel synthesis. It was observed that the NCNTs were completely and homogeneously coated with QMMOs/TiO<sub>2</sub> nanoparticles. The photoluminescence emission peaks of NCNTs containing NCNTs were lower than that of the QMMOs and TiO<sub>2</sub>, indicating retardation of the recombination of the electrons and holes. The photocatalytic efficiencies of the materials were tested by monitoring the efficiency at which they photodegraded BPA under visible-light irradiation ( $\lambda > 400$  nm). The QMMOs had higher photocatalytic efficiency relative to that of TiO<sub>2</sub>. The photocatalytic efficiency of QMMOs increased with decreasing amounts of W<sup>6+</sup> incorporated into TiO<sub>2</sub>. The photocatalytic efficiency of TiO<sub>2</sub> was not improved by much when was loaded onto NCNTs (TiO<sub>2</sub>/10% NCNTs) but that of the QMMOs loaded on NCNTs was significantly increased. These remarks ratify that incorporation of W<sup>6+</sup> and Zn<sup>2+</sup> and compositing the materials with TiO<sub>2</sub> resulted in unique materials with the potential of being viable photocatalysis.

## Conflicts of interest

There are no conflicts of interest to declare.

## Acknowledgements

This work is built on the research funded in part by the National Research Foundation (NRF) of South Africa (Grant number 88076), ESCOM's Tertiary Education Support Programme (TESP) and the DST-NRF Centre of Excellence in Strong Materials (CoE-SM) at the University of the Witwatersrand. The authors would also like to thank our colleagues who were somewhat involved in this work, including Mr Tiisetso Moimane, Miss Gugulethu Nkala and Miss Phuledi Mphago.

## References

- 1 A. Fujishima and K. Honda, *Nature*, 1972, **238**, 37–38.
- 2 Z. Huang, Q. Sun, K. Lv, Z. Zhang, M. Li and B. Li, *Appl. Catal., B*, 2015, **164**, 420–427.
- 3 F. Dziike, P. J. Franklyn, S. H. Durbach, M. Maubane and L. Hlekelele, *Mater. Res. Bull.*, 2018, **104**, 220–226.
- 4 Z. Zheng, B. Huang, J. Lu, Z. Wang, X. Qin, X. Zhang, Y. Dai and M.-H. Whangbo, *Chem. Commun.*, 2012, **48**, 5733–5735.
- 5 Z. Zheng, B. Huang, J. Lu, X. Qin, X. Zhang and Y. Dai, *Chem.–Eur. J.*, 2011, **17**, 15032–15038.
- 6 A. Naldoni, M. Allieta, S. Santangelo, M. Marelli, F. Fabbri, S. Cappelli, C. L. Bianchi, R. Psaro and V. Dal Santo, *J. Am. Chem. Soc.*, 2012, **134**, 7600–7603.
- 7 M. K. Nowotny, L. R. Sheppard, T. Bak and J. Nowotny, *J. Phys. Chem. C*, 2008, **112**, 5275–5300.
- 8 T. D. Nguyen-Phan and E. W. Shin, *J. Ind. Eng. Chem.*, 2011, **17**, 397–400.
- 9 F. He, J. Li, T. Li and G. Li, *Chem. Eng. J.*, 2014, **237**, 312–321.
- 10 A. Fernández, G. Lassaletta, V. M. Jiménez, A. Justo, A. R. González-Elipe, J. M. Herrmann, H. Tahiri and Y. Ait-Ichou, *Appl. Catal., B*, 1995, **1–2**, 49–63.
- 11 P. Huo, Y. Yan, S. Li, H. Li and W. Huang, *Desalination*, 2010, **256**, 196–200.
- 12 R. J. Tayade, R. G. Kulkarni and R. V. Jasra, *Ind. Eng. Chem. Res.*, 2007, **46**, 369–376.
- 13 D. Hazarika and N. Karak, *Appl. Surf. Sci.*, 2016, **376**, 276–285.
- 14 R. Leary and A. Westwood, *Carbon*, 2011, **49**, 741–772.
- 15 B. Gao, G. Z. Chen and G. Li Puma, *Appl. Catal., B*, 2009, **89**, 503–509.
- 16 L. Hlekelele, P. J. Franklyn, F. Dziike and S. H. Durbach, *New J. Chem.*, 2018, **42**, 1902–1912.
- 17 V. Vaiano, O. Sacco, D. Sannino and P. Ciambelli, *Appl. Catal., B*, 2015, **170–171**, 153–161.
- 18 C. Shen, K. Pang, L. Du and G. Luo, *Particuology*, 2017, **34**, 103–109.
- 19 L. Hlekelele, P. J. Franklyn, F. Dziike and S. H. Durbach, *New J. Chem.*, 2018, **42**, 4531–4542.
- 20 B. Wang, Q. Li, W. Wang, Y. Li and J. Zhai, *Appl. Surf. Sci.*, 2011, **257**, 3473–3479.
- 21 A. Di Paola, G. Marci, L. Palmisano, M. Schiavello, K. Uosaki, S. Ikeda and B. Ohtani, *J. Phys. Chem. B*, 2002, **3**, 637–645.
- 22 M. A. Rauf, M. A. Meetani and S. Hisaindee, *Desalination*, 2011, (1–3), 13–27.
- 23 C. He, Y. Yu, X. Hu and A. Larbot, *Appl. Surf. Sci.*, 2002, (1–4), 239–247.
- 24 X. Fu, J. Long, X. Wang, D. Leung, Z. Ding, L. Wu, Z. Zhang, Z. Li and X. Fu, *Int. J. Hydrogen Energy*, 2008, **33**, 6484–6491.
- 25 V. Iliiev, D. Tomova, S. Rakovsky, A. Eliyas and G. L. Puma, *J. Mol. Catal. A: Chem.*, 2010, **327**, 51–57.
- 26 M. Ni, M. K. H. Leung, D. Y. C. Leung and K. Sumathy, *Renewable Sustainable Energy Rev.*, 2007, **11**, 401–425.
- 27 H. Tada, T. Kiyonaga and S. I. Naya, *Chem. Soc. Rev.*, 2009, **7**, 1849–1858.



- 28 Q. Zhang, W. Li, C. Moran, J. Zeng, J. Chen, L. P. Wen and Y. Xia, *J. Am. Chem. Soc.*, 2010, **132**, 11372–11378.
- 29 T. Hirakawa, *J. Am. Chem. Soc.*, 2005, **127**, 3928–3934.
- 30 F. Wu, X. Hu, J. Fan, E. Liu, T. Sun, L. Kang, W. Hou, C. Zhu and H. Liu, *Plasmonics*, 2013, **8**, 501–508.
- 31 M. Dahl, Y. Liu and Y. Yin, *Chem. Rev.*, 2014, **114**, 9853–9889.
- 32 Z. Zhang, W. Wang, L. Wang and S. Sun, *ACS Appl. Mater. Interfaces*, 2012, **4**, 593–597.
- 33 G. G. Ying, R. S. Kookana and P. Dillon, *Water Res.*, 2003, **37**, 3785–3791.
- 34 Y. R. Do, W. Lee, K. Dwight and A. Wold, *J. Solid State Chem.*, 1994, **108**, 198–201.
- 35 S. Y. Chai, Y. J. Kim and W. I. Lee, *J. Electroceram.*, 2006, **2–4**, 909–912.
- 36 H. Fu, T. Xu, S. Zhu and Y. Zhu, *Environ. Sci. Technol.*, 2008, **42**, 8064–8069.
- 37 T. T. Vu, L. del Río, T. Valdés-Solís and G. Marbán, *Appl. Catal., B*, 2013, **140–141**, 189–198.
- 38 F. X. Xiao, *ACS Appl. Mater. Interfaces*, 2012, **4**, 7055–7063.
- 39 B. M. Rajbongshi, S. K. Samdarshi and B. Boro, *J. Mater. Sci.: Mater. Electron.*, 2015, **26**, 377–384.
- 40 P. Franklyn, *Hydrothermal synthesis and characterisation of titania nanoparticles*, University of the Witwatersrand, 2004.
- 41 R. Asahi, Y. Taga, W. Mannstadt and A. Freeman, *Phys. Rev. B: Condens. Matter Mater. Phys.*, 2000, **61**, 7459–7465.
- 42 D. O. Scanlon, C. W. Dunnill, J. Buckeridge, S. A. Shevlin, A. J. Logsdail, S. M. Woodley, C. R. A. Catlow, M. J. Powell, R. G. Palgrave, I. P. Parkin, G. W. Watson, T. W. Keal, P. Sherwood, A. Walsh and A. A. Sokol, *Nat. Mater.*, 2013, **12**, 798–801.
- 43 R. Sanjinés, H. Tang, H. Berger, F. Gozzo, G. Margaritondo and F. Lévy, *J. Appl. Phys.*, 1994, **75**, 2945.
- 44 P. J. Franklyn and A. Narrandes, *Proceedings of the International Conference Nanomaterials: Applications and Properties*, 2012, **1**, 1–17.
- 45 L. Hlekelele, P. Tripathi, P. J. Franklyn and S. H. Durbach, *RSC Adv.*, 2016, **6**, 76773–76779.
- 46 P. J. Franklyn, *Synthesis, characterisation and structural investigations of nanoparticulate forms of selected (W, Ti, Al, Ba) mixed metal oxides*, Univ. Cambridge, 2011.
- 47 S. D. Perera, R. G. Mariano, K. Vu, N. Nour, O. Seitz, Y. Chabal and K. J. Balkus, *ACS Catal.*, 2012, **2**, 949–956.
- 48 L. Wang, L. Shen, Y. Li, L. Zhu, J. Shen and L. Wang, *Int. J. Photoenergy*, 2013, **2013**, 1–7.
- 49 N. Hintsho, L. Petrik, A. Nechaev, S. Titinchi and P. Ndungu, *Appl. Catal., B*, 2014, **156–157**, 273–283.
- 50 K. Woan, G. Pyrgiotakis and W. Sigmund, *Adv. Mater.*, 2009, **21**, 2233–2239.
- 51 O. Avilés-García, J. Espino-Valencia, R. Romero, J. L. Rico-Cerda, M. Arroyo-Albiter and R. Natividad, *Fuel*, 2017, **198**, 31–41.
- 52 A. Gutiérrez-Alejandre, J. Ramírez and G. Busca, *Catal. Lett.*, 1998, **56**, 29–33.
- 53 P. Benjwal and K. K. Kar, *RSC Adv.*, 2015, **5**, 98166–98176.
- 54 F. Dzikke, P. J. Franklyn, L. Hlekelele and S. H. Durbach, *Diamond Relat. Mater.*, 2019, **99**, 107519.
- 55 A. Bianco Prevot, M. Vincenti, A. Bianciotto and E. Pramauro, *Appl. Catal., B*, 1999, **22**, 149–158.

